This is a preprint, the final version is subject to change, of the American Mineralogist (MSA)
Cite as Authors (Year) Title. American Mineralogist, in press.
DOI: https://doi.org/10.2138/am-2020-7355

Revision 2

Crystal-chemistry and microfeatures in gadolinite imprinted by pegmatite formation and alteration evolution

Nenad Tomašić[1], Radek Škoda[2], Vladimir Bermanec[1], Marin Šoufek[3]

[1]University of Zagreb, Faculty of Science, Department of Geology, Horvatovac 102a, HR-10000 Zagreb, Croatia, ntomasic@geol.pmf.hr, vberman@public.carnet.hr

[2]Masaryk University, Faculty of Science, Department of Geological Sciences, Kotlařska 2, CZ-61137 Brno, Czech Republic, rskoda@sci.muni.cz

[3]Croatian Natural History Museum, Demetrova 1, HR-10000 Zagreb, Croatia

marin.soufek@gmail.com

Abstract

Gadolinite [$REE_2Fe^{2+}Be_2Si_2O_{10}$] is a common mineral in certain types of REL-REE pegmatites. Changes in pegmatite environment during and after gadolinite formation could be devised by studying its crystal-chemical properties and a thorough observation of microfeatures in the mineral matrix. Post-crystallization processes in pegmatite might trigger alteration mechanisms in gadolinite like in other REE-rich pegmatite minerals, whereby various late-magmatic or metasomatic events may affect mineral chemistry. Three gadolinite samples originating from various pegmatite occurrences in southern Norway offer an excellent insight in post-crystallization evolution of the pegmatites; by studying their crystallographic, chemical and micro-textural features, imprints of the related processes in the pegmatites were devised in this

study. Relevant mineral information was collected in recrystallization experiments of fully or slightly metamictized gadolinite samples and subsequent XRD analyses. Micro-Raman spectroscopy, EMPA and SEM-BSE-EDS analyses were employed to retrieve micro-chemical properties and related micro-textural features of the mineral matrix. With a reference to the gadolinite supergroup, a general alteration path can be envisaged outlining the pegmatite evolution and suggesting the occurrence of the secondary REE mineral phases: altered gadolinite domains prove Ca enrichment with a tendency towards hingganite composition, while a slight fluorine increase and sporadic secondary fluorite occurrence point out a significant role of fluorine as a complexing agent in dissolution-reprecipitation mechanism of metasomatic alteration in the mineral. Micro-Raman spectra show an improved vibration statistics for the altered gadolinite domains, which could be well-related to Ca substituting REE and a possible increase of structural ordering within the gadolinite structure, being at the same time an indication of structural healing of metamictized domains by metasomatic processes. A study of microfeatures in the complex silicates like gadolinite proves to be an excellent tool to trace post-crystallization processes in a pegmatitic environment. With a slight redistribution of radionuclides during alteration in gadolinite observed, a moderate precaution has to be taken in a case of selecting gadolinite for dating within U-Th-Pb system.

Keywords: Gadolinite-(Y), crystal-chemical properties, metamictization, alteration domains, metasomatism, pegmatites

Introduction

Gadolinite is a REE silicate with a formula $REE_2Fe^{2+}Be_2Si_2O_{10}$**.** Three mineral species share the generic mineral name: gadolinite-(Y), gadolinite-(Ce) and gadolinite-(Nd). They are mutually distinguished by dominant REE cation at the A position in the structure. A new nomenclature was recently approved by IMA (Hålenius et al. 2016; Bačík et al. 2017) establishing the gadolinite supergroup that is defined by a general formula $A_2MQ_2T_2O_8\varphi_2$, where A = Ca, REE, Pb, Mn^{2+}, Bi (C.N. 8), M = Fe^{2+}, □, Mg, Mn, Zn, Cu, Al (C.N. 6), Q = Be, B, Li (C.N. 4), T = Si, P, As, B, Be, S (C.N. 4), and φ = O, OH, F. The gadolinite supergroup is divided into the gadolinite and herderite group on a basis of T-site occupancy (Si versus As/P, respectively). The gadolinite group is further subdivided into the gadolinite and datolite subgroup with Be and B occupying Q site, respectively, or at the same time, divalent cations occupying A-site in the datolite subgroup and trivalent ones in the gadolinite subgroup. Gadolinite frequently occurs metamictized but when crystallized, it is monoclinic with S.G. $P2_1/a$ (Miyawaki et al. 1984).

Occurrences of the gadolinite subgroup minerals are traditionally reported in granitic pegmatites of REL-REE subclass (Černy and Ercit 2005) or syenite pegmatites associated with larvikite magma (Segalstad and Larsen 1978). More recently, secondary gadolinite findings were described as a product of late-magmatic, post-magmatic and alteration processes in granitoids and metamorphic environments (Uher et al. 2009; Majka et al. 2011), whereby gadolinite could have been evolved from primary REE minerals like allanite-(Ce), monazite-(Ce) or xenotime-(Y). Gadolinite has been also reported from Bastnäs-type Fe-REE deposits (Holtstam and Andersson 2007; Škoda et al. 2018).

Early studies of gadolinite and other REE minerals were often related to their scarce occurrence, complex crystal-chemical properties, which were especially characterized by frequent metamictization (Malczewski 2010). Recent studies commonly address alteration in REE-bearing minerals as a potential source of information for post-magmatic, metasomatic and metamorphic processes in pegmatite and host rocks. The alteration of REE-bearing minerals in the pegmatites has been especially well-documented in the case of common orthophosphates like monazite and xenotime (Williams et al. 2011; Harlov 2011; Harlov et al. 2011; Seydoux-Guillaume et al. 2012; Švecová et al. 2016).

In gadolinite samples from three different pegmatite areas of southern Norway chemical and phase inhomogeneity was observed on micro-scale. Therefore, the samples were investigated for their crystal-chemical properties and textural microfeatures like intergrowths and mineral alterations within the specimens. The basic idea of the study was to relate structural and chemical features of unaltered and altered/non-gadolinite domains in the samples and to establish a connection to possible post-crystallization processes occurring in pegmatitic systems. Additionally, some of the observed features might be related to the geological setup of particular pegmatite hosting the investigated mineral sample.

Geological background

The investigated gadolinite samples originate from three different pegmatites, which are situated in southern Norway and characterized by their own geological and mineralogical features (Fig. 1).

The Hidra pegmatite is situated on the island of Hidra, and intrudes anorthosite/leuconorite of the Rogaland Igneous Complex. The Rogaland complex is hosted by

gneisses of the Sveconorwegian ages (Hetherton and Harlov 2008) to which the magmatic suite does not show obvious connection. Pasteels et al. (1979) reported an age of 937 ± 4 Ma that was obtained by U-Pb dating on zircon, monazite, titanite and uraninite. The Hidra pegmatite veins are 1-15 m thick comprising massive quartz, albite crystals, books of muscovite and biotite, magnetite, xenotime, monazite in large plagioclase and K-feldspars, allanite-(Ce), aeschynite-(Y), and kainosite-(Y). Graphic textures frequently occur.

The Kåbuland pegmatite belongs to the famous Evje-Iveland pegmatite field. The field is up 10 km wide and 30 km long with several hundred major pegmatite bodies emplaced into amphibolite gneisses, metanorites and metadiorites (Pedersen et al. 2009). With an estimated thickness of 15 m, the Kåbuland pegmatite does not display a distinct zoning as observed at the opened outcrop. A mineral assemblage is composed of quartz, K-feldspar, plagioclase, biotite, magnetite, allanite-(Ce), aeschynite-(Y), polycrase-(Y), fergusonite-(Y) and xenotime-(Y). The pegmatite can be classified to REL-REE allanite-monazite/euxenite sub-class (Snook 2013). Various ages have been reported for the Evje-Iveland pegmatite field and accompanying rocks (Pedersen and Konnerup-Madsen 1994, 2000): 1290 Ma for augen gneiss (Rb/Sr in whole rock), 1278 ± 2Ma for norite (U/Pb in zircon), and 950 - 900 Ma for granite-monzonite. Interestingly, a reported age of 910 ± 1.6 Ma for an unknown pegmatite was obtained by using U/Pb dating in a sample of gadolinite (Scherer et al. 2001).

The Høydalen pegmatite is situated in the Tørdal pegmatite field, from which the third investigated gadolinite sample was recovered. The sample originates from the upper Høydalen pegmatite, which is described as amazonite-bearing and intrudes coarse-grained metamorphized gabbroic rocks. The pegmatite dykes are up to 4-5 m broad, and contain K-feldspar partly replaced by *cleavelandite*, mica (muscovite to *lepidolite*), beryl, topaz, cassiterite, molybdenite etc. (Raade et al. 1993, Rosing-Schow et al. 2018). The locality is renowned for a great variety of

119 REE minerals, and it is type locality of tveitite-(Y). The age is approximately 900 Ma (Segalstad
120 and Eggleston 1993).
121
122 **Materials and methods**
123
124 In this paper, definition of rare-earth elements group follows recommendation of IUPAC
125 (International Union for Pure and Applied Chemistry). The term rare-earth elements (REE)
126 includes lanthanides (Ln), yttrium (Y), and scandium (Sc). Due to the substantially smaller ionic
127 radius of Sc with respect to the rest of the group, it frequently enters different crystal-structural
128 sites via different substitutions, and therefore, Sc is commonly not included as a REE in
129 geological sciences, and neither in this paper. Because of the lanthanide contraction phenomenon,
130 the REE are further divided into larger LREE (light Ln, La–Gd) and smaller HREE (heavy Ln,
131 Tb–Lu). Yttrium is grouped together with HREE due to chemical similarities.
132 All three samples were carefully inspected by stereo microscope and only pieces of
133 apparently pure gadolinite were selected for X-ray powder diffraction analysis. The samples were
134 ground in agate mortar and analyzed by a Philips X'Pert PRO powder diffractometer using
135 sample spinner at revolution time of 1 rev/s. A silicon zero-background plate was used as a
136 sample holder, thus improving signal to noise ratio. The diffractometer was powered by 45 kV
137 and 40 mA generating CuKα radiation (λ = 1.54178 Å). Soller slits, divergence slit of ¼°, anti-
138 scatter slit of ½°, receiving slit of 1° and proportional detector were inserted into the
139 diffractometer geometry setup. Initial X-ray scanning showed that gadolinite samples from
140 Kåbuland and Høydalen were metamict but for the sake of consistency, all three samples were
141 heated at 400, 500, 650, 800 and 1000°C in air for 24 hours to gradually recover/heal gadolinite

142 structure. After each heating step the samples were X-rayed applying the same instrument
143 settings as described before. The obtained XRD patterns were analyzed using X´Pert HighScore
144 ver. 2.0. The patterns presenting recovered gadolinite structure were indexed and unit-cell
145 parameters calculated. Intensity and full width at half maximum (FWHM) were measured for the
146 gadolinite *112* reflection (when observed) to monitor recrystallization progress. Pseudo-Voight
147 function was used to fit the diffraction maximum.

148 Raman spectra were obtained for the thermally untreated samples from polished sections
149 mounted on glass slide by means of a Horiba Labram HR Evolution spectrometer. This
150 dispersive, edge-filter-based system is equipped with an Olympus BX 41 optical microscope, a
151 diffraction grating with 600 grooves per millimeter, and a Peltier-cooled, Si-based charge-
152 coupled device (CCD) detector. After careful tests with different lasers (473, 532 and 633 nm),
153 the 633 nm He-Ne laser with the beam power of 10 mW at the sample surface was selected for
154 spectra acquisition to minimize analytical artefacts. Raman signal was collected in the range of
155 100–4000 cm^{-1} with a 100x objective and the system being operated in the confocal mode, beam
156 diameter was ~1 μm and the lateral resolution ~2 μm. No visual damage of the analyzed surface
157 was observed at these conditions after the excitation. Wavenumber calibration was done using the
158 Rayleigh line and low-pressure Ne-discharge lamp emissions. The wavenumber accuracy was
159 ~0.5 cm^{-1}, and the spectral resolution was ~2 cm^{-1}. Afterwards, the sample chips were embedded
160 in epoxy resin, additionally fine-polished and used for electron microprobe analysis (EMPA).

161 Prior to the EMPA analysis the samples were carbon coated (Sputter Coater Bal-Tec SCD
162 050) and inspected by scanning electron microscope (SEM) Tescan Vega MM5136 as well as
163 with Tescan FE SEM MIRA 2 LMU equipped with Bruker EDS QUANTAX 200 employing 129

eV XFlash Detector 5010. The samples were checked for homogeneity and microfeatures like mineral inclusions or gadolinite alteration.

Cameca SX 100 microprobe was used for EMPA. The accelerating potential was 15 keV, the current 20 nA and beam diameter 5 μm. A whole range of WDS spectrometers was employed (PET, LPET, LLIF, TAP, PC1). The following standards were used with selected lines for measurement in parentheses: albite (Na*K*α), hematite (Fe*K*α), spessartine (Mn *K*α), $NdPO_4$ (Nd *L*β), $PrPO_4$ (Pr *L*β), $LaPO_4$ (La *L*α), $CePO_4$ (Ce *L*α), anatase (Ti *K*α), sanidine (Si *K*α, Al *K*α), YPO_4 (Y *L*α), $SmPO_4$ (Sm *L*β), $DyPO_4$ (Dy *L*β), $GdPO_4$ (Gd *L*β), $ErPO_4$ (Er *L*α), wollastonite (Ca *K*α), $CaTh(PO_4)_2$ (Th *M*α), U (U *M*β), topaz (F *K*α), Mg_2SiO_4 (Mg *K*α), zircon (Zr *L*α), $ScVO_4$ (Sc *K*α), fluorapatite (P *K*α.), $SrSO_4$ (Sr *L*α), $TbPO_4$ (Tb *L*α), $HoPO_4$ (Ho *L*β), $YbPO_4$ (Yb *L*α), vanadinite (Pb *M*α)(*below detection limit), $TmPO_4$ (Tm *L*α), $EuPO_4$ (Eu *L*β). The raw data, including a theoretical content of Be, were processed using the X-PHI matrix correction routine (Merlet 1994). Based on the counting statistics, the measurement error expressed as 2σ is approximately <1 rel% for concentrations around 20 wt% and ~8 rel% for concentrations around 1 wt%. To minimize spectral interferences, careful WDS angle scans of gadolinite were performed prior to the analyses in order to set the proper analytical lines and background positions for REE analysis. An empirically determined correction factor was applied to the coincidence of Ce *M*ζ , 2^{nd} order of Dy *M*β and 3^{rd} order Y *L*β with the F *K*α line, Tb *L*β,β_4 with the Er *L*α line, Sm *L*γ with the Tm *L*α, and Tb *L*β_2 with the Yb *L*α line (see Škoda et al. 2015). Gadolinite formulae were based on the fixed number of Si = 2, and a theoretical BeO content was computed on stoichiometric basis of 2 Be per formula unit.

Results and discussion

Structural properties – do they facilitate gadolinite alteration?

XRD patterns of the thermally untreated samples show that the samples from Høydalen and Käbuland are severely metamictized, though very weak major diffraction maxima could be distinguished from characteristic amorphous broadening in the pattern. Both samples gradually recrystallized with the gadolinite crystal structure upon heating experiments with annealing temperature increased in each subsequent annealing step. Related XRD patterns for the two samples are very similar, and those of the Høydalen sample are presented in Figure 2 in order to depict typically observed recrystallization path. The final heating product in cases of both samples is gadolinite, and no other phases were observed in XRD patterns. The recrystallization path of these two samples corresponds to a partially metamict gadolinite characterized by direct recrystallization, as described by Janeczek and Eby (1993). Unlike some other complex silicate minerals prone to metamictization like allanite (Čobić et al. 2010), gadolinite structure shows ability to recover from radiation damage even in the atmospheric conditions. The unheated sample from Hidra yielded diffraction pattern of a non-metamict gadolinite. However, in order to determine slight changes in the crystal structure due to possible short-range radiation damage, the Hidra sample was also subjected to the heating experiments. Unit cell parameters were calculated for the unheated (RT) and heated samples (Table 1), with a larger standard deviation for the unheated samples from Høydalen and Käbuland due to their generally metamict appearance in the diffraction patterns and only a few diffraction lines available for the calculation. The recrystallization process was monitored by measuring intensity of the gadolinite *112* line (one of the strongest gadolinite diffraction maxima) and its FWHM value (Fig. 3). If unit cell volume is assumed to be an average measure of unit cell changes during heating experiments, a slight

211 increase of the values is observed for all the samples in the temperature range up to 500-650°C.
212 With further increase of temperature the unit cell volume starts to behave a bit differently for the
213 three samples: it drops in all three samples at 650°C and a further decrease is recorded for the
214 Hidra sample as recrystallization temperature rises. In two other samples, however, the volume
215 starts to increase again. The average change between initial (unheated) and final (1000°C) unit
216 cell volume varies less than 1%, which compares well with the similar observations for the
217 gadolinite samples of various crystallinity annealed in atmosphere and hydrothermally (Janeczek
218 and Eby 1993). The temperature of 650° as an approximate start of recrystallization seems to
219 correlate well with the observations from similar recrystallization studies. Lima de Faria (1964)
220 pointed out that early studies of many metamict minerals had shown recrystallization commenced
221 around 600°C. Indeed, he managed to recrystallize gadolinite at 700°C after 3 hours of heating
222 for most of his gadolinite samples, having achieved the same result after heating them for 1 hour
223 at 1000°C. However, at higher recrystallization temperatures the structure recovery was
224 successful for all the investigated samples. This suggests time could play a certain role in the
225 recrystallization of gadolinite, and a prolonged heating at lower temperatures can yield
226 recrystallized structure. However, initial degree of metamictization seems to influence the
227 success of the structure recovery at a lower heating temperature, which was also shown in the
228 study of Janeczek and Eby (1993). A newer study of a partially metamict gadolinite sample
229 (Paulmann et al. 2019) suggests local recrystallization at 670°C, a better ordered crystalline
230 structure at 711°C and structure recovery at 800°C.
231 The observed departure in trend of the unit cell change in the middle of the
232 recrystallization temperature range is also indicated by measuring FWHM values and intensities
233 of *112* diffraction line. This phenomenon can be related to slight adjustments of recrystallizing
234 domains in the mineral as well as to water removal, usually immanent for the mineral domains

with damaged structure (Ewing 1994). Also, additional rearrangements are possible due to dissolution-reprecipitation processes, which resulted in the chemically altered domains, a part of which could have had different state of crystallinity in comparison with the metamictized domains (see later discussion).

Micro-Raman spectra for the thermally untreated samples are presented in Figure 4. The observed bands are assigned to bending and stretching modes as follows: ν_1 – symmetric stretching, ν_2 – symmetric bending, ν_3 – asymmetric stretching, and ν_4 – asymmetric bending. This assignment largely follows the band attribution for nesosilicates (Farmer 1974; Kloprogge and Frost 2000; Zhang et al. 2000). The bands do not entirely coincide in all three samples; nevertheless, two band ranges occur in all of them: 360-375 cm^{-1} (symmetric bending modes) and 870-890 cm^{-1} (symmetric stretching modes). As these bands could be also observed in two severely metamictized samples (Kåbuland and Høydalen), they could indicate local structure preservation. These preserved domains in a metamict matrix might have induced straightforward recovery of gadolinite original structure by playing a role of recrystallization centers for an epitaxial growth (Wang et al. 2000; Tomašić et al. 2010). An increase of band intensity and/or resolution for these fundamental vibrations was recorded in the altered, Ca-rich domains (datolite component) of the gadolinite samples. This is likely to be caused by the substitution of Ca for REE, which can improve vibration statistics of some vibration bands. Namely, a higher content of REE in unaltered areas can produce a spread of vibration frequencies in the observed vibration modes owing to a wider range of interatomic distances caused by a range of ionic radii for REE. Since the observed bands are related to Si-O internal vibrations of SiO_4 tetrahedra, this influence of REE content in the crystal structure should be treated more as a lattice vibration net effect. Lattice vibrations are affected by vibrations of neighboring atoms and translational symmetry of

258 atoms in crystal structure (McMillan and Hofmeister 1988). External lattice vibrations (here, the
259 vibrations of atoms surrounding SiO_4 group as well as the movements of entire SiO_4 group within
260 crystal structure) can to a certain extent influence internal SiO_4 vibration modes in nesosilicate
261 gadolinite (Nasdala et al. 2004). So, they should be sensitive to a range of substitutions in A-site.
262 On the other hand, the recorded response of Raman spectra to the replacement of REE by Ca in
263 the altered domains could compare well with Bačik et al. (2014), who found that an increase in
264 layer stacking-order could have been suggested for more datolitic composition, i.e. shifting of A-
265 site occupancy toward more Ca-enriched. This would also mean that hydrothermal alteration
266 increases internal structural order in altered domains, mainly due to the REE removal.
267 Additionally, formation of Ca-enriched gadolinite by dissolution-reprecipitation mechanism
268 could have locally annihilated the impact of radiation damage in gadolinite with reprecipitated
269 domains not suffering from metamictization effects significantly, and thus yielding more defined
270 vibration modes (Nasdala et al. 1995).
271 The results of chemical analysis and calculated cation assignment are presented in Table
272 2. All three samples turned out to be gadolinite-(Y). Overall content of U and Th is quite low
273 (roughly in the range 0.2-0.7% on oxide basis or 0.002-0.013 per formula unit). However, it
274 seems to be sufficient to trigger severe metamictization in two out of three samples.
275 Concentrations of Th and U in the Hidra sample, which is the only one proven non-metamict in
276 XRD experiments, are lower when compared to the sample from Kåbuland with roughly double
277 the content. Yet the sample from Høydalen has significantly less U, although generally exceeding
278 Th content of the Hidra sample. Thus, the sum of radionuclides is even lower than in the Hidra
279 sample. This could indicate another crystal-chemical constraint for the stability of the crystal
280 structure in the Hidra sample and/or an event which could have induced crystal structure recovery
281 in the sample. With generally low radionuclide content, gadolinite metamictization could have

282 been triggered by crystal-chemical constraints mostly imparted by a complex crystal structure
283 outline. All cation positions in the gadolinite structure can accommodate a range of various
284 cations that are different in ionic radius and sometimes in charge. For instance, the largest A-site
285 is particularly interesting in this respect. Raman spectra of the altered domains suggest that
286 introduction of Ca could stabilize the structure. Ionic radii of several LREE that are close to the
287 radius of Ca^{2+} (La-Nd) (Shannon 1976) could probably play similar role. Refinement of the
288 gadolinite crystal structure (Miyawaki et al. 1984) shows a significant distortion of the
289 coordination polyhedron around A-site cations, with a dispersion of cation-oxygen interatomic
290 distances ranging from 2.329 to 2.691 Å. Y is the dominant cation in this site (ionic radius 1.019
291 Å), and calculation of the polyhedron stability for its 8-fold coordination, which is based on Y/O
292 ionic radius ratio, yields values that are below the standard stability threshold (< 0.732) if some
293 of the Y-O bond distances are taken into consideration. When Ca (ionic radius 1.120 Å) enters A-
294 site, this ratio improves and the coordination polyhedron stabilizes. By observing metamictization
295 in complex Nb and Ta oxides, Graham and Thornber (1974) proposed that metamictization was a
296 result of segregation into domains of different structure and/or composition, and the presence of
297 radionuclides in the structure expectedly accelerated this disproportionation. The complexity of
298 gadolinite structure could cause an excessive strain in the structure making it less stable and more
299 susceptible to metamictization. Metamictization, on the other hand, triggers chemical changes
300 and hence mineral alterations due to an increased chance for elements to redistribute or leach out
301 of a mineral (Tomašić et al. 2008; Geisler et al. 2002).

302 In summary, the metamictized gadolinite samples show a gradual recrystallization path
303 starting in temperature range 500-650°C, and no other phases emerge during the process. The
304 collected crystal-chemical evidences from the studied samples indicate a certain mineral
305 susceptibility to alteration. Micro-Raman spectra of the altered domains supplemented by

306 microchemical data suggest an enhancement of crystallinity due to increase of Ca content.
307 Indirectly, Raman spectra appear to be sensitive to Ca incorporation in A-site (largely occupied
308 by REE in gadolinite), which seems to reduce effects of metamictization in locally altered
309 domains.
310
311 **Inhomogeneity of the samples: tracing a post-crystallization evolution**
312 A thorough inspection of the samples using SEM-BSE-EDS setup reveals inhomogeneity
313 in all three samples (Figs. 5a-5g). They are observed either as inclusions of other minerals in
314 gadolinite matrix or alteration domains of gadolinite itself.
315 By observing general appearance of the inclusions, these can be regarded either primary
316 or secondary. For instance, in the Hidra sample K-feldspar and fluorite display an anhedral
317 outline. K-feldspar generally fills up crevices (Fig. 5f), which could indicate its formation in a
318 later stage of pegmatite evolution after the crystallization of gadolinite. On the other hand,
319 inclusion of plagioclase in the Høydalen sample (Fig. 5c) with a typical euhedral habit suggests it
320 co-crystallized with gadolinite. This could imply that gadolinite had crystallized in an earlier
321 stage of pegmatite formation and was later altered by remaining pegmatite melt or late magmatic
322 fluids evolving from solidifying pegmatite (Hetherington and Harlov 2008). Alteration of the
323 Høydalen gadolinite is clearly visible in Figures 5c and 5d as darker grey stripes that are
324 regularly separated by unaltered gadolinite. Observation at higher magnification (Fig. 5d) reveals
325 altered areas along tiny crevices. Chemical mapping of plagioclase, on the other hand, does not
326 show any alteration changes in plagioclase chemistry, with a very sharp chemical boundary
327 between plagioclase and gadolinite.
328 Respectable domains in all three samples seem to have been altered, and alteration zones
329 mainly follow fractures and crevices (Fig. 5b, 5d, 5g). Thus, an alteration path along these

330 microtextures could have been established by percolating metasomatic fluids. The following
331 alteration patterns can be recognized on a basis of chemical variations among pristine and altered
332 domains in gadolinite:
333 1. Loss in U and Th accompanied with a gain in REE and Ca, with some of the altered domains
334 approaching hingganite composition (Kåbuland sample; Fig. 5b). Some of the adjacent domains
335 indicate slightly different cation redistribution on an alteration path causing loss in REE, Fe and
336 U, and gain in Th, Ca, Na (Altered domains 2).
337 2. Loss in REE, Fe, U and Th, and concomitant gain in Ca and Na (Hidra and Høydalen; Figs. 5d,
338 5g). The alteration pattern is quite similar to the latter case depicted for the Kåbuland sample,
339 with exemption of Th behavior.
340 3. Loss in Y and Fe coupled by a gain in U, Th, REE-Y (REE excluding Y), and Ca. This is
341 observed in the case of Hidra sample (Fig. 5g, Alteration domains 1), and is characterized by a
342 gain in actinides within altered domains and no related loss in vicinal unaltered areas.
343 4. A slight increase of fluorine in all three samples, being the least prominent in Høydalen, and
344 most pronounced in Hidra with an occurrence of F-bearing phase (fluorite).
345 Considering the observed alteration-driven changes of gadolinite chemistry, following
346 substitution vectors could be assumed:
347 1. $REE^{3+} + Fe^{2+} \leftrightarrow Ca^{2+} + Fe^{3+}$,
348 for which a spatial-sensitive determination of Fe^{2+}/Fe^{3+} would be required to devise extent of this
349 substitution. The observed change of chemistry indicates depletion of Fe in pristine domains,
350 which are more likely to accommodate Fe^{2+} since Fe^{3+} is not readily incorporated in the
351 gadolinite structure prior to the recrystallization (Malczewski 2010) or even after annealing
352 (Paulmann et al. 2019).
353 2. $Fe^{2+} + REE^{3+} + 3O^{2-} \leftrightarrow Ca^{2+} + \square + 3(OH^-,F^-)$,

354 The observation of chemistry in the alteration domains supports this exchange mechanism
355 resulting in Ca and F increase. In the case of Hidra sample a significant availability of fluorine in
356 the system is suggested by occurrence of fluorite. Previous findings by Hetherington & Harlov
357 (2008) assumed a small fluorine contribution as a complexing agent for REE removal in altered
358 domains of monazite and xenotime at the locality, however, fluorine might have played a more
359 significant role in gadolinite in this respect. It should be noted that gadolinite-datolite and
360 gadolinite-hingganite relations can be expressed as follows, respectively: $Fe^{2+}+ 2REE^{3+} + 2Be^{2+}$
361 $+ 2O^{2-} \leftrightarrow \square + 2Ca^{2+} + 2B^{3+} + 2OH^{-}$, and $Fe^{2+} + 2O^{2-} \leftrightarrow \square + 2OH^{-}$.
362 3. $REE^{3+} + U^{4+} \leftrightarrow Ca^{2+} + Na^{+} + Th^{4+}$,
363 This alteration mechanism was observed in the case of Kåbuland sample (Altered domains 2),
364 indicating a selective actinide behavior due to alkali/earth-alkali presence in alteration fluids.
365 4. $REE^{3+} + Be^{2+} \leftrightarrow Ca^{2+} + B^{3+}$
366 To determine the extent of this substitution, a detailed structural refinement of the altered
367 domains is required. Alternatively, a microspatial chemical analysis of light elements, which is
368 usually difficult to achieve using standard laboratory equipment, would be appropriate. Bearing
369 in mind that in the gadolinite supergroup Ca-dominant members usually accommodate B rather
370 than Be, and the observed alteration domains indeed acquire Ca during alteration processes,
371 introduction of B in the structure could be assumed provided its availability in the system. Also,
372 formula calculations show a certain deficiency of Be and other cations in some altered areas
373 (Table 2), which could be surely attributed to the incorporation of boron.
374 Generally all alteration mechanism previously considered presume incorporation of Ca.
375 Similar processes have been observed in the case of complex Nb, Ta and Ti rare earth oxides
376 which are also prone to alteration during metamictization, frequently ending up with pyrochlore

group minerals as a product (Ercit 2005). Thus, complex crystal structures incorporating REE seem to be likely to replace REE with Ca during metasomatic reactions promoted by hydrothermal fluids in late/post-magmatic pegmatitic systems. This could be a mechanism of reducing structural strain by incorporating a single element with similar ionic radius but different charge, and the crystal structure recovery as evidenced by micro-Raman spectra.

Occurrence of minute $ThSiO_4$ domains is observed only in the case of Kåbuland sample, and only as a rare phenomenon. In contrast to monazite or xenotime (Hetherington and Harlov 2008; Harlov et al. 2011; Seydoux-Guillaume et al. 2012), in which $ThSO_4$ inclusions are plentiful in alteration domains, a low magnitude of the $ThSiO_4$ occurrence in gadolinite can be easily related to much lower abundancy of Th in the gadolinite structure. Also, the only observed inclusion in gadolinte (Fig 5a, inset) does not appear to be a part of an alteration domain, so one can also assume a probability of its crystallization due to a local Th enrichment.

Almost all electron microprobe analyses yielded a gadolinite composition (Fig. 6). However, a tendency towards a hingganite composition could be observed for altered domains. This is indicated by introduction of more Ca in the A-site of the crystal structure and slight impoverishment of REE. At the same time, the sum of M site cations decreases accounting merely for a loss of Fe.

REE distribution in the gadolinite samples (Fig. 7) with chondrite normalized values indicates an enrichment of HREE in both unaltered and altered domains, as could be expected from Y prevalence among REE in the investigated samples. When REE distribution in unaltered and altered domains is compared, the following observations could be made:

1. LREE do not change significantly in all three samples.
2. HREE change slightly more prominently featuring following trends:

a) For Kåbuland and Hidra samples a minute enrichment is observed in certain altered relative to unaltered domains; this is especially the case for the domains with composition shifted to the hingganite compositional field (Kåbuland sample).
b) In Hidra sample fractionation of HREE seems to be the lowest among three samples; this can be related to different geological setup of Hidra area hosting gadolinite-bearing pegmatites, which is associated with anorthosite complex. Another two areas, Kåbuland and Høydalen, are related to more fractioned melts evolved from partial melting within metamorphic complex of Evje Iveland area during Sweconorwegian movements (Müller et al. 2012).
c) Høydalen sample shows the most prominent difference among unaltered and altered domains displaying impoverishment of HREE in altered domains, but their distribution pattern follows the one of the unaltered domains.

3. Strong negative Eu anomaly in all three samples indicates advanced fractionation of parent melts. Altered domains in the Kåbuland sample gained some Eu, which could have entered the crystal structure together with Ca during metasomatism. Since unaltered domains show Eu abundances below detection limit, the recorded increase of Eu could be related to accumulation of Eu at particular areas during several cycles of dissolution-reprecipitation process, which pushed Eu content within detection limit. BSE-EDS observation indicated that altered areas with strong REE depletion and those with some REE enrichment are placed at very close distances within the sample (Fig. 5b, Alteration domains 1 and 2). Microstructrual features, which could have caused “Eu anchoring” in this case, could be related to distribution of metamictized vs. structurally preserved domains in the mineral matrix.

Altogether, investigation of microfeatures in the studied gadolinite samples revealed evidences of post-crystallization processes in a form of mineral inclusions and domains of altered gadolinite. The altered domains, occurring around fractures and crevices in the samples, are characterized by several alteration patterns. A common feature of all the patterns is enrichment of Ca in A-position of the gadolinite structure, which is usually coupled with some actinide impoverishment in two metamictized samples and ambiguous REE behavior. Thus, the altered domains show a tendency toward hingganite composition. Fluorine is found to play a significant role during metasomatic alteration processes in gadolinite. Change of REE distribution in altered relative to unaltered domains is slightly more pronounced for HREE. Eu anomaly is strongly negative, but several altered domains seem to have gained some Eu, possibly together with Ca enrichment due to crystal-chemical constraints and repeated cycles of dissolution-reprecipitation.

Implications

Gadolinite unlike many metamict minerals can be easily recrystallized in simple heating experiments run in uncontrolled atmosphere. Only a small amount of radionuclides in a very complex structure seem to be sufficient enough to trigger metamictization, which compares gadolinite well with zircon. A study of microfeatures in the gadolinite samples from the pegmatites of southern Norway revealed alteration domains, which generally lost some of their REE by replacement with Ca. Micro-Raman spectra indicated structural ordering and probably healing in dissolution-reprecipitation mechanism of metasomatic alteration, thus attributing Ca as a structure-stabilizer in the altered domains of the metamictized gadolinite. This process resembles pyrochloritization in complex REE-Nb-Ta-Ti oxides, in which an increase of alkali and earth-alkali elements occurs on expense of leaking REE. Slight increase of fluorine in altered

447 domains and fluorite in gadolinite matrix point out a significant role of fluorine in metasomatic
448 alteration processes within gadolinite.

449 With gadolinite as a role model, REE minerals with complex composition and crystal
450 structure prove to be a useful indicator of post-crystallization processes, since their structures
451 seem to be very sensitive and responsive to alteration processes like metasomatism. Especially
452 studying mineral microfeatures promotes itself as an excellent tool to trace these processes in a
453 mineral.

454 During alteration of gadolinite, actinide mobility is hereby confirmed, and dating using U-
455 Th-Pb system requires precaution when selecting suitable gadolinite domains for the analysis.
456 Micro-Raman analysis along several profiles in individual sections of metamictized gadolinite
457 can distinguish the domains with increased band intensities and resolution implying their
458 improved crystallinity. In some cases, these spectral features could indicate preserved domains of
459 the original crystal structure, but also, as shown in this study, chemically altered regions in the
460 sample. The latter can be confirmed by an increased Ca content and usually concomitant U-Th-
461 Pb impoverishment.

462

463 **Acknowledgments**

464 The authors are grateful to the Mineralogical Museum of the University in Oslo and Mr Gunnar
465 Raade, retired curator, who provided the gadolinite samples. We thank Prof. Aaron S. Bell for his
466 suggestions and comments that helped to improve this paper. The work was supported by the
467 scientific grant 20282401of the University in Zagreb and a research program of Masaryk
468 University MUNI/A/1479/2019.

469

470

References cited

Bačík, P., Fridrichová, J., Uher, P., Pršek, J., and Ondrejka, M. (2014) The crystal chemistry of gadolinite-datolite group series. Canadian Mineralogist, 52, 625-642.

Bačík, P., Miyawaki, R., Atencio, D., Cámara, F., and Fridrichová, J. (2017) Nomenclature of the gadolinite supergroup. European Journal of Mineralogy, 29, 1067-1082.

Bergstol, S., and Juve, G. (1988) Scandian ixiolite, pyrochlore and bazzite in granite pegmatite in Tordal, Telemark, Norway. A contribution to the mineralogy and geochemistry of scandium and tin. Mineralogy and Petrology, 38, 229-243.

Bjørlykke, H. (1930) Blomstrandin von Kåbuland. Norsk Geologisk Tidsskrift, 11, 232-239.

Bugge, J.A.W. (1978) Norway. In S.H.U. Bowie, A. Kvalheim, and H.W. Haslam, Eds., Mineral Deposits of Europe, Volume 1: Northwest Europe, p. 199-249. The Institution of Mining and Metallurgy, The Mineralogical Society, London.

Cámara, F., Oberti, R., Ottolini, L., Della Ventura, G., and Bellatreccia, F. (2008) The crystal chemistry of Li in gadolinite. American Mineralogist, 96, 996-1004.

Černý, P., and Ercit, T.S. (2005) The classification of granitic pegmatites revisited. Canadian Mineralogist, 43, 2005-2026.

Čobić, A., Bermanec, V., Tomašić, N., and Škoda, R. (2010) The hydrothermal recrystallization of metamict allanite-(Ce). Canadian Mineralogist, 48, 513-521.

Demartin, F., Minglia, A., and Gramaccioli, C.M. (2001) Characterization of gadolinite-group minerals using crystallographic data only: The case of hingganite-(Y) from Cuasso al Monte, Italy. Canadian Mineralogist, 39, 1105-1115.

Demartin, F., Pilati, T., Diella, V., Gentle, P., and Gramaccioli, C.M. (1993) A crystal-chemical investigation of alpine gadolinite. Canadian Mineralogist, 30, 127-136.

Ercit, T.S. (2005) Identification and alteration trends of graniticpegmatite-hosted (Y,REE,U,Th)-(Nb,Ta,Ti) oxide minerals: astatistical approach. Canadian Mineralogist, 43, 1291–1303.

Ewing, R.C. (1994) The metamict state: 1993 - the centennial. Nuclear Instruments and Methods in Physics Research, B91, 22-29.

Farmer V.C. (1974) The infrared spectra of minerals, p. 539, Mineralogical Society Monograph 4, Mineralogical Society, London.

Geisler, T., Pidgeon, R.T., Bronswijk, W., and Kurtz, R. (2002) Transport of uranium, thorium, and lead in metamict zicron under low-temperature hydrothermal conditions. Chemical Geology, 191, 141-154

519 Graham, J., and Thornber, M.R: (1974): The crystal chemistry of complex niobium and tantalum
520 oxides IV. The metamict state. American Mineralogist, 59, 1047-1050.
521
522 Hålenius, U., Hatert, F., Pasero, and Mills, M.S.J. (2016) New minerals and nomenclature
523 modifications approved in 2016, IMA Commission on New Minerals, Nomenclature and
524 Classification (CNMNC) - Newsletter 33. Mineralogical Magazine, 80, 1135-1144.
525
526 Harlov, D.E. (2011) Formation of monazite and xenotime inclusions in fluorapatite megacrysts,
527 Gloserheia Granite Pegmatite, Froland, Bamble Sector, southern Norway. Mineralogy and
528 Petrology, 102, 77-86.
529
530 Harlov, D.E, Wirth, R., and Hetherington, C.J. (2011) Fluid-mediated partial alteration in
531 monazite: the role of coupled dissolution–reprecipitation in element redistribution and mass
532 transfer. Contributions to Mineralogy and Petrology, 162, 329-348.
533
534 Hetherington, C.J., and Harlov, D.E. (2008) Metasomatic thorite and uraninite inclusions in
535 xenotime and monazite from graniticpegmatites, Hidra anorthosite massif, southwestern Norway:
536 Mechanics and fluid chemistry. American Mineralogist, 93, 806-820.
537
538 Holtstam, D., and Andersson, U.B. (2007) The REE minerals of the Bastnas-type deposits, south-
539 central Sweden. The Canadian Mineralogist, 45(5), 1073-1114.
540
541 Janeczek, J., and Eby, R.K. (1993) Annealing of radiation damage in allanite and gadolinite.
542 Physics and Chemistry of Minerals, 19, 343-356.

Kloprogge, J.T., and Frost, R.L. (2000) Raman microscopic study at 300 and 77 K of some pegmatite minerals from the Iveland-Evje area, Aust-Agder, Southern Norway. Spectrochimica Acta Part A, 56, 501-513.

Lima de Faria, J. (1964) Identification of metamict minerals by X-ray powder photographs. Estudos, Ensaios e Documentos, 112, 74 p. Junta de Investigaçoes do Ultramar, Lisboa.

Macdonald, R., Bagiński, ., Kartashov, P.M., and Zozulya, D. (2017) Behaviour of $ThSiO_4$ during hydrothermal alteration of rare-metal rich lithologies from peralkaline rocks. Mineralogical Magazine, 81, 873-893.

Majka, J., Pršek, J., Budzyn, B., Bačik, P., Barker, A.K., and Łodzinski, M. (2011) Fluorapatite-hingganite-(Y) coronas as products of fluid-induced xenotime-(Y) breakdown in the Skoddefjellert pegmaitete, Svalbard. Mineralogical Magazine, 75, 159-167.

Malczewski, D. (2010) Recrystallization in fully metamict gadolinite from Ytterby (Sweden), annealed in air and studied by ^{57}Fe Mössbauer spectroscopy. American Mineralogist, 95, 463-471.

McMillan, P.F., and Hofmeister, A.M. (1988) Infrared and Ramam spectroscopy. In F.C. Hawthorne, Ed., Spectroscopic Methods in Mineralogy and Geology, 18, p. 99-159. Reviews in Mineralogy and Geochemistry, Mineralogical Society of America, Washington, D.C.

Merlet, C. (1994) An accurate computer correction program for quantitative electron microprobe analysis. Microchimica acta, 114/115, 363-376.

Miyawaki, R., Nakai, I., and Nagashima, K. (1984) A refinement of the crystal structure of gadolinite. American Mineralogist, 69, 948-953.

Müller, A., Kearsley, A., Spratt, J., and Seltmann, R. (2012) Petrogenetic implications of magmatic garnet in granitic pegmatites from Southern Norway. Canadian Mineralogist, 50, 1095-1115.

Nasdala, L., Irmer, L., and Wolf, D. (1995) The degree of metamictization in zircon: a Raman spectroscopic study. European Journal of Mineralogy, 7, 471– 478.

Nasdala, L., Smith, D.C., Kaindl, R., and Ziemann, M.A. (2004) Raman spectroscopy: Analytical perspectives in mineralogical research. In A. Beran and E. Libowitzky, Eds., Spectroscopic Methods in Mineralogy, 6, p. 281-343. Notes in Mineralogy, European Mineralogical Union, Budapest.

Nijland, T.G., Harlov, D.E., and Andersen, T. (2014) The Bamble Sector, South Norway: A review. Geoscience Frontiers, 5, 635-658.

Pasteels, P., Demaiffe, D., and Michot, J. (1979) U-Pb and Rb-Sr geochronology of the eastern part of the south Rogaland igneous complex, southern Norway. Lithos, 12, 199–208.

591 Paulmann, C., Zietlow, P., McCammon, C., Salje, E.K.H., and Bismayer, U. (2019) Annealing of
592 metamict gadolinite-(Y): X-ray diffraction, Raman, IR, and Mössbauer spectroscopy. Zeitschrift
593 für Kristallographie – Crystalline Materials (in press).
594
595 Pedersen, S., and Konnerup-Madsen, J. (1994) Geology of the Setesdal Region. Excursion Guide
596 to the SNF Excursion, August 1994, pp. 55. Copenhagen University, Copenhagen.
597
598 Pedersen, S., and Konnerup-Madsen, J. (2000) Geology of the Setesdalen area, South Norway:
599 Implications for the Sveconorwegian evolution of South Norway. Bulletin of the Geological
600 Society of Denmark, 46, 181–201.
601
602 Pedersen, S., Andersen, T., Konnerup-Madsen, J., and Griffin, W.L. (2009) Recurrent
603 Mesoproterozoic continental magmatism in south-central Norway. International Journal of Earth
604 Sciences, 98, 1151-1171.
605
606 Perchiazzi, N., Gualtieri, A.F., Merlino, S., and Kampf, A.R. (2004) The atomic structure of
607 bakerite and its relationship to datolite. American Mineralogist, 89, 767-776.
608
609 Pršek, J., Ondrejka, M., Bačik, P., Budzyn, B., and Uher, P. (2010) Metamorphic-hydrothermal
610 REE minerals in the Bacúch magnetite deposit, Western Carpathians, Slovakia: (Sr,S)-rich
611 monazite-(Ce) and Nd-dominant hingganite. Canadian Mineralogist, 48, 81-94.
612

613 Raade, G., Sæbo, P.Ch., Austrheim, H., and Kristiansen, R. (1993) Kuliokoite-(Y) and its
614 alteration products kainosite-(Y) and kamphaugite-(Y) from granite pegmatite in Tørdal,
615 Norway. European Journal of Mineralogy, 5, 691-698.
616
617 Rinaldi, R., Gatta, G.D., and Angel, R.J. (2010) Crystal chemistry and low-temperature behavior
618 of datolite: A single-crystal X-ray diffraction study. American Mineralogist, 95, 1413-1421.
619
620 Rosing-Schow, N., Müller, A., and Friis, H. (2018) A comparison of the mica geochemistry of
621 the pegmatite fields in southern Norway. The Canadian Mineralogist, 56, 463-488.
622
623 Scherer, E., Münker, C., and Mezger, K. (2001) Calibration of the lutetium–hafnium clock.
624 Science, 293, 683-687.
625
626 Segalstad, T., and Eggleston, T. (1993) Pegmatittene i Tørdal, Telemark. Stein, 20, 190-195.
627
628 Segalstand, T., and Larsen, A.O. (1978) Gadolinite-(Ce) from Skien, southwestern Oslo region,,
629 Norway. American Mineralogist, 63, 188-195.
630
631 Seydoux-Guillaume, A.M., Montel, J.M., Bingen, B., Bosse, V., de Parseval, P., Paquette, J.L.,
632 Janots, E., and Wirth, R. (2012) Low-temperature alteration of monazite: Fluid mediated coupled
633 dissolution–precipitation, irradiation damage, and disturbance of the U–Pb and Th–Pb
634 chronometers. Chemical Geology, 330-331, 140-158.
635

636 Shannon, R.D. (1976) Revised Effective Ionic Radii and Systematic Studies of Interatomic
637 Distances in Halides and Chalcogenides. Acta Crystallographica Section A, 32, 751–767.
638
639 Snook, B.R. (2013) Towards exploration tools for high purity quartz: an example from the South
640 Norwegian Evje-Iveland pegmatite belt, p. 258, PhD. thesis, University of Exeter, Exeter.
641
642 Škoda, R., Plášil, J., Jonsson, E., Čopjaková, R., Langhof, J., and Galiová, M.V. (2015)
643 Redefinition of thalénite-(Y) and discreditation of fluorthalénite-(Y): A re-investigation of type
644 material from the Österby pegmatite, Dalarna, Sweden, and from additional localities.
645 Mineralogical Magazine, 79(4), 965-983.
646
647 Škoda, R., Plášil, J., Čopjaková, R., Novák, M., Jonsson, E., Galiová, M. V., and Holtstam, D.
648 (2018) Gadolinite-(Nd), a new member of the gadolinite supergroup from Fe-REE deposits of
649 Bastnäs-type, Sweden. Mineralogical magazine, 82(S1), S133-S145.
650
651 Švecová, E., Čopjaková, R., Losos, Z., Škoda, R., Nasdala, L., and Cícha, J. (2016) Multi-stage
652 evolution of xenotime–(Y) from Písek pegmatites, Czech Republic: an electron probe micro-
653 analysis and Raman spectroscopy study. Mineralogy and Petrology, 110, 747-765.
654
655 Tomašić, N., Bermanec, V., Gajović, A., and Rajić Linarić, M. (2008) Metamict minerals: an
656 insight into a relic crystal structure using XRD, Raman spectroscopy, SAED and HRTEM.
657 Croatica Chemica Acta, 81, 391-400.
658

659 Tomašić, N., Gajović, A., Bermanec, V., Rajić Linarić, M., Su, D., and Škoda, R. (2010)
660 Preservation of the samarskite structure in a metamict ABO4 mineral: a key to crystal structure
661 identification. European Journal of Mineralogy, 22, 435-442.
662
663 Uher, P., Ondrejka, M., and Konečný, P. (2009) Magmatic and post-magmatic Y-REE-Th
664 phosphate, silicate and Nb-Ta-Y-REE oxide minerals in A-type metagranite: an example from the
665 Turčok massif, the Western Carpathians, Slovakia. Mineralogical Magazine, 73, 1009-1025.
666
667 Wakita, H., Ray, P., and Schmit, R.A. (1971) Abundances of 14 rare-earth elements and 12 other
668 trace elements in Apollo 12 samples: Five igneous and one breccia rocks and four soils.
669 Proceeding of the Second Lunar Science Conference, Volume 2, p. 1319-1329, The M.I.T. Press.
670
671 Wang, S.X., Wang, L.M., and Ewing, R.C. (2000) Nano-scale glass formation in pyrochlore by
672 ion irradiation. Journal of Non-Crystalline Solids, 274, 238–243.
673
674 Williams, M.L., Jercinovic, M.J., Harlov, D.E., Budzyń, B., and Hetherington, C.J. (2011)
675 Resetting monazite ages during fluid-related alteration. Chemical Geology, 283, 218-225.
676
677 Zhang, M., Salje, E.K.H., Capitani, G.C., Leroux, H., Clark, A.M., Schlüter, J., and Ewing, R.C.
678 (2000) Annealing of α-decay damage in zircon: a Raman spectroscopic study. Journal of Physics:
679 Condensed Matter, 12, 3131-3148.
680
681

682 **Figure captions**

683

684 **Figure 1.** Location of hosting pegmatite bodies for the investigated gadolinite samples with
685 simplified geological outline after Bugge (1978).

686

687 **Figure 2.** XRD recrystallization pattern of the Høydalen sample showing a typical
688 straightforward recrystallization pattern for a metamict gadolinite.

689

690 **Figure 3.** Impact of recrystallization on *112* diffraction line parameters: intensities vs. FWHM in
691 the investigated samples of gadolinite.

692

693 **Figure 4.** Micro-Raman spectra recorded on unaltered and altered domains in gadolinite (band
694 assignment labels: ν_1 – symmetric stretching, ν_2 – symmetric bending, ν_3 – asymmetric
695 stretching, ν_4 – asymmetric bending; references in the text).

696

697 **Figure 5.** BSE images of the gadolinite samples depicting various inhomogeneity patterns
698 observed at microscopic scale: (**a-b**) Kåbuland, (**c-d**) Høydalen, (**e1-e4**) plagioclase within
699 Høydalen gadolinite – element map for Na, Al, Y and Fe, (**f-g**) Hidra.

700

701 **Figure 6.** A compositional diagram for the EMPA analyses of the gadolinite samples investigated
702 and indication of an alteration path shifting slightly a gadolinite to a hingganite composition
703 (classification diagram of the gadolinite group after Bačík et al. 2017).

704

Figure 7. Chondrite-normalized REE distribution diagrams for unaltered (solid lines) and altered (dashed lines) gadolinite-(Y) samples investigated (chondrite values after Wakita et al. 1971). Lu abundances are always under detections limit and thus not presented in the diagram. Y values are always the highest, but for atomic number consistency not shown. To emphasize delicate differences among REE distribution of unaltered and altered domains logarithmic scale was not applied in this case.

This is a preprint, the final version is subject to change, of the American Mineralogist (MSA)
Cite as Authors (Year) Title. American Mineralogist, in press.
DOI: https://doi.org/10.2138/am-2020-7355

713 **Table 1.** Unit cell parameters calculated for unheated (RT) and the gadolinite samples heated at
714 recrystallization temperatures (standard deviations in parentheses)

715

Sample	t (°C)	a (Å)	b (Å)	c (Å)	β (°)	V (Å^3)
Kåbuland	RT	9.92(2)	7.57(2)	4.75(1)	90.8(1)	356.8(8)
	400	9.92(1)	7.495(7)	4.744(4)	90.6(1)	352.6(3)
	500	9.95(2)	7.67(1)	4.91(1)	91.07(9)	374.6(6)
	650	9.966(8)	7.52(1)	4.721(6)	90.10(9)	353.9(4)
	800	9.944(3)	7.514(2)	4.715(2)	89.96(3)	352.3(2)
	1000	9.9637(9)	7.5155(7)	4.7404(7)	90.01(1)	354.97(6)
Høydalen	RT	9.81(5)	7.50(2)	4.80(2)	90.9(2)	353(1)
	400	9.80(6)	7.63(4)	4.77(2)	90.6(5)	357(2)
	500	10.00(2)	7.500(8)	4.81(1)	89.5(3)	361(1)
	650	9.904(5)	7.521(5)	4.717(3)	90.20(4)	351.3(1)
	800	9.943(4)	7.505(4)	4.735(4)	90.16(5)	353.3(2)
	1000	9.964(1)	7.5177(6)	4.7397(8)	90.01(2)	355.04(6)
Hidra	RT	9.939(8)	7.489(9)	4.742(4)	90.57(8)	352.9(5)
	400	9.91(1)	7.52(1)	4.737(6)	90.7(1)	353.1(5)
	500	9.974(5)	7.544(6)	4.762(3)	90.44(6)	358.3(3)
	650	10.002(2)	7.539(1)	4.743(1)	90.47(1)	357.60(7)
	800	9.970(1)	7.534(1)	4.734(2)	90.14(3)	355.6(1)
	1000	9.949(2)	7.5130(8)	4.734(1)	90.06(3)	353.8(1)

716

This is a preprint, the final version is subject to change, of the American Mineralogist (MSA)
Cite as Authors (Year) Title. American Mineralogist, in press.
DOI: https://doi.org/10.2138/am-2020-7355

717 **Table 2.** EMPA chemical composition of the gadolinite samples and cation assignment (bdl – below detection limit, 0.000 = < 0.001)

	Kåbuland							**Hidra**								**Høydalen**				
	unaltered			altered				unaltered			altered					unaltered			altered	
	1	2	3	4	5	6	7	8	9	10	11	12	13	14	15	16	17	18	19	20
	Chemical composition (in wt%)																			
SiO_2	24.69	24.68	24.65	24.72	24.74	26.51	24.61	24.49	24.60	24.59	24.64	23.27	24.55	24.60	32.80	24.59	24.37	24.33	24.73	24.23
Al_2O_3	bdl	bdl	bdl	bdl	bdl	bdl	bdl	bdl	bdl	bdl	bdl	bdl	bdl	bdl	0.71	bdl	bdl	bdl	bdl	bdl
ThO_2	0.43	0.42	0.44	0.24	0.44	0.25	0.55	0.13	0.11	0.12	0.11	0.09	0.20	0.10	0.30	0.19	0.20	0.13	0.30	0.26
UO_2	0.21	0.22	0.21	bdl	0.21	bdl	0.19	0.20	0.20	0.18	0.27	0.20	0.31	0.25	bdl	0.08	bdl	bdl	bdl	bdl
Y_2O_3	35.50	35.64	35.36	35.79	35.21	38.62	33.02	34.66	35.02	35.65	35.33	32.19	32.02	33.13	20.66	32.78	32.53	32.97	30.07	29.35
La_2O_3	0.18	0.15	0.25	bdl	0.28	bdl	0.20	0.42	0.51	0.43	0.41	0.40	0.27	0.28	0.23	0.16	0.16	bdl	0.19	bdl
Ce_2O_3	1.37	1.35	1.35	1.35	1.18	0.96	1.20	2.46	2.34	2.17	2.20	2.38	2.80	1.91	1.07	0.92	0.84	0.89	0.91	0.91
Pr_2O_3	0.35	0.29	0.34	0.32	0.32	0.30	0.32	0.55	0.47	0.61	0.51	0.53	0.78	0.46	0.26	0.24	0.31	0.19	0.34	0.31
Nd_2O_3	1.87	1.85	2.23	2.03	1.90	1.66	1.86	2.49	2.47	2.17	2.41	2.57	3.48	2.12	1.28	1.67	1.65	1.58	1.67	1.70
Sm_2O_3	0.87	0.74	0.75	0.91	0.79	0.85	0.81	0.63	0.70	0.64	0.61	0.62	1.26	0.63	0.45	1.16	1.32	1.13	1.06	1.20
Eu_2O_3	bdl	bdl	bdl	bdl	bdl	0.37	bdl	bdl	bdl	bdl	bdl	bdl	bdl	bdl	bdl	bdl	bdl	bdl	bdl	bdl
Gd_2O_3	2.50	2.47	2.46	2.52	2.31	2.52	2.39	1.57	1.63	1.61	1.59	1.75	2.55	1.55	1.34	3.73	3.75	3.39	3.16	3.38
Tb_2O_3	0.35	0.33	0.36	0.29	0.37	0.39	0.33	0.17	bdl	0.17	0.23	0.17	0.39	bdl	0.12	0.56	0.59	0.51	0.45	0.44
Dy_2O_3	2.86	2.91	2.64	2.93	3.05	3.16	2.73	2.06	2.11	2.12	2.06	1.98	3.20	1.94	1.75	4.08	4.02	4.01	3.63	3.68
Ho_2O_3	0.47	0.52	0.59	0.62	0.60	0.48	0.52	0.38	0.39	0.40	0.46	0.43	0.66	0.51	0.26	0.77	0.81	0.81	0.75	0.64
Er_2O_3	1.95	1.97	1.98	2.02	2.01	2.30	1.83	1.73	1.72	1.82	1.76	1.73	2.48	1.67	1.45	2.75	2.64	2.70	2.51	2.41
Tm_2O_3	0.40	0.26	0.31	0.34	0.38	0.47	0.32	0.30	0.30	0.31	0.27	0.29	0.44	0.22	0.31	0.48	0.50	0.47	0.46	0.45
Yb_2O_3	2.21	2.14	2.25	2.20	2.23	2.58	2.07	2.36	2.31	2.46	2.39	2.19	2.70	2.26	2.12	2.86	2.79	3.05	2.77	2.73
CaO	0.08	0.06	0.09	0.14	0.11	0.21	1.59	0.15	0.10	0.09	0.11	0.15	0.24	1.06	0.54	0.07	0.05	0.06	0.67	0.33
MgO	bdl	bdl	bdl	bdl	0.04	bdl	bdl	bdl	bdl	bdl	bdl	bdl	bdl	bdl	bdl	bdl	0.06	0.04	0.04	bdl
MnO	0.28	0.32	0.30	0.30	0.33	bdl	0.35	0.25	0.30	0.30	0.33	0.28	0.21	0.22	0.14	0.28	0.28	0.35	0.37	0.22
FeO	13.74	13.54	13.77	13.65	13.33	5.17	10.92	13.83	13.94	13.92	13.87	12.29	8.46	10.70	9.68	12.95	12.90	13.09	11.43	12.13
Na_2O	bdl	bdl	bdl	bdl	bdl	bdl	0.12	bdl	bdl	bdl	bdl	bdl	bdl	0.40	bdl	bdl	bdl	bdl	0.07	bdl
F	bdl	bdl	bdl	bdl	bdl	bdl	0.03	bdl	bdl	bdl	0.07	0.05	0.39	0.45	0.77	bdl	bdl	bdl	<0.01	<0.01
BeO*	10.28	10.27	10.26	10.29	10.30	11.03	10.25	10.19	10.24	10.23	10.26	9.69	10.22	10.24	13.66	10.24	10.14	10.13	10.29	10.08
Total	100.6	100.1	100.6	100.6	100.1	97.80	96.23	99.03	99.45	99.99	99.87	93.25	97.59	94.70	89.89	100.5	99.89	99.83	95.87	94.47

This is a preprint, the final version is subject to change, of the American Mineralogist (MSA)
Cite as Authors (Year) Title. American Mineralogist, in press.
DOI: https://doi.org/10.2138/am-2020-7355

	Kåbuland							**Hidra**								**Høydalen**				
	unaltered			altered				unaltered			altered					unaltered			altered	
	1	2	3	4	5	6	7	8	9	10	11	12	13	14	15	16	17	18	19	20
	Number of atoms per formula unit based on 2Si																			
Si	2.000	2.000	2.000	2.000	2.000	2.000	2.000	2.000	2.000	2.000	2.000	2.000	2.000	2.000	2.000	2.000	2.000	2.000	2.000	2.000
Al	0.000	0.000	0.000	0.000	0.000	0.000	0.000	0.000	0.000	0.000	0.000	0.000	0.000	0.000	0.051	0.000	0.000	0.000	0.000	0.000
Th	0.008	0.008	0.008	0.004	0.008	0.004	0.010	0.002	0.002	0.002	0.002	0.002	0.004	0.002	0.004	0.003	0.004	0.002	0.005	0.005
U	0.004	0.004	0.004	0.000	0.004	0.000	0.003	0.004	0.004	0.003	0.005	0.004	0.006	0.005	0.000	0.002	0.000	0.000	0.000	0.000
Y	1.530	1.537	1.527	1.541	1.515	1.551	1.428	1.507	1.515	1.543	1.526	1.472	1.388	1.433	0.670	1.419	1.421	1.442	1.294	1.289
La	0.005	0.005	0.007	0.000	0.008	0.000	0.006	0.013	0.015	0.013	0.012	0.013	0.008	0.008	0.005	0.005	0.005	0.000	0.006	0.000
Ce	0.041	0.040	0.040	0.040	0.035	0.026	0.036	0.074	0.070	0.065	0.065	0.075	0.083	0.057	0.024	0.027	0.025	0.027	0.027	0.027
Pr	0.010	0.008	0.010	0.010	0.010	0.008	0.010	0.016	0.014	0.018	0.015	0.017	0.023	0.014	0.006	0.007	0.009	0.006	0.010	0.009
Nd	0.054	0.054	0.065	0.059	0.055	0.045	0.054	0.073	0.072	0.063	0.070	0.079	0.101	0.062	0.028	0.049	0.048	0.046	0.048	0.050
Sm	0.024	0.021	0.021	0.025	0.022	0.022	0.023	0.018	0.020	0.018	0.017	0.018	0.035	0.018	0.009	0.033	0.037	0.032	0.030	0.034
Eu	0.000	0.000	0.000	0.000	0.000	0.009	0.000	0.000	0.000	0.000	0.000	0.000	0.000	0.000	0.000	0.000	0.000	0.000	0.000	0.000
Gd	0.067	0.066	0.066	0.068	0.062	0.063	0.064	0.043	0.044	0.043	0.043	0.050	0.071	0.042	0.027	0.100	0.102	0.092	0.085	0.093
Tb	0.009	0.009	0.010	0.008	0.010	0.010	0.009	0.004	0.000	0.005	0.006	0.005	0.010	0.000	0.002	0.015	0.016	0.014	0.012	0.012
Dy	0.075	0.076	0.069	0.076	0.080	0.077	0.071	0.054	0.055	0.056	0.054	0.055	0.084	0.051	0.034	0.107	0.106	0.106	0.095	0.098
Ho	0.012	0.013	0.015	0.016	0.015	0.012	0.013	0.010	0.010	0.010	0.012	0.012	0.017	0.013	0.005	0.020	0.021	0.021	0.019	0.017
Er	0.050	0.050	0.050	0.051	0.051	0.055	0.047	0.044	0.044	0.046	0.045	0.047	0.063	0.043	0.028	0.070	0.068	0.070	0.064	0.065
Tm	0.010	0.006	0.008	0.008	0.010	0.011	0.008	0.008	0.007	0.008	0.007	0.008	0.011	0.006	0.006	0.012	0.013	0.012	0.012	0.012
Yb	0.055	0.053	0.056	0.054	0.055	0.059	0.053	0.059	0.057	0.061	0.059	0.057	0.067	0.056	0.039	0.071	0.070	0.076	0.068	0.069
Ca	0.007	0.005	0.007	0.012	0.009	0.017	0.139	0.013	0.008	0.008	0.009	0.013	0.021	0.092	0.035	0.006	0.004	0.006	0.061	0.029
Mg	0.000	0.000	0.000	0.000	0.005	0.000	0.000	0.000	0.000	0.000	0.000	0.000	0.000	0.000	0.000	0.000	0.007	0.005	0.005	0.000
Mn	0.019	0.022	0.021	0.020	0.023	0.000	0.024	0.018	0.021	0.021	0.022	0.021	0.015	0.016	0.007	0.019	0.020	0.024	0.025	0.016
Fe	0.931	0.918	0.934	0.923	0.901	0.326	0.742	0.945	0.948	0.947	0.941	0.883	0.577	0.727	0.494	0.881	0.885	0.900	0.773	0.837
Na	0.000	0.000	0.000	0.000	0.000	0.000	0.019	0.000	0.000	0.000	0.000	0.000	0.000	0.063	0.000	0.000	0.000	0.000	0.011	0.000
F	0.000	0.000	0.000	0.000	0.000	0.000	0.001	0.000	0.000	0.000	0.002	0.001	0.011	0.012	0.023	0.000	0.000	0.000	0.001	0.001
Be*	2.000	2.000	2.000	2.000	2.000	2.000	2.000	2.000	2.000	2.000	2.000	2.000	2.000	2.000	2.000	2.000	2.000	2.000	2.000	2.000
A site	1.961	1.955	1.963	1.972	1.952	1.969	1.992	1.941	1.938	1.963	1.947	1.926	1.991	1.963	0.924	1.945	1.957	1.957	1.849	1.807
M site	0.950	0.940	0.955	0.943	0.924	0.326	0.766	0.962	0.969	0.968	0.964	0.904	0.591	0.743	0.552	0.900	0.905	0.924	0.798	0.853

*BeO content calculated on basis of 2Be per formula unit

Figure 1

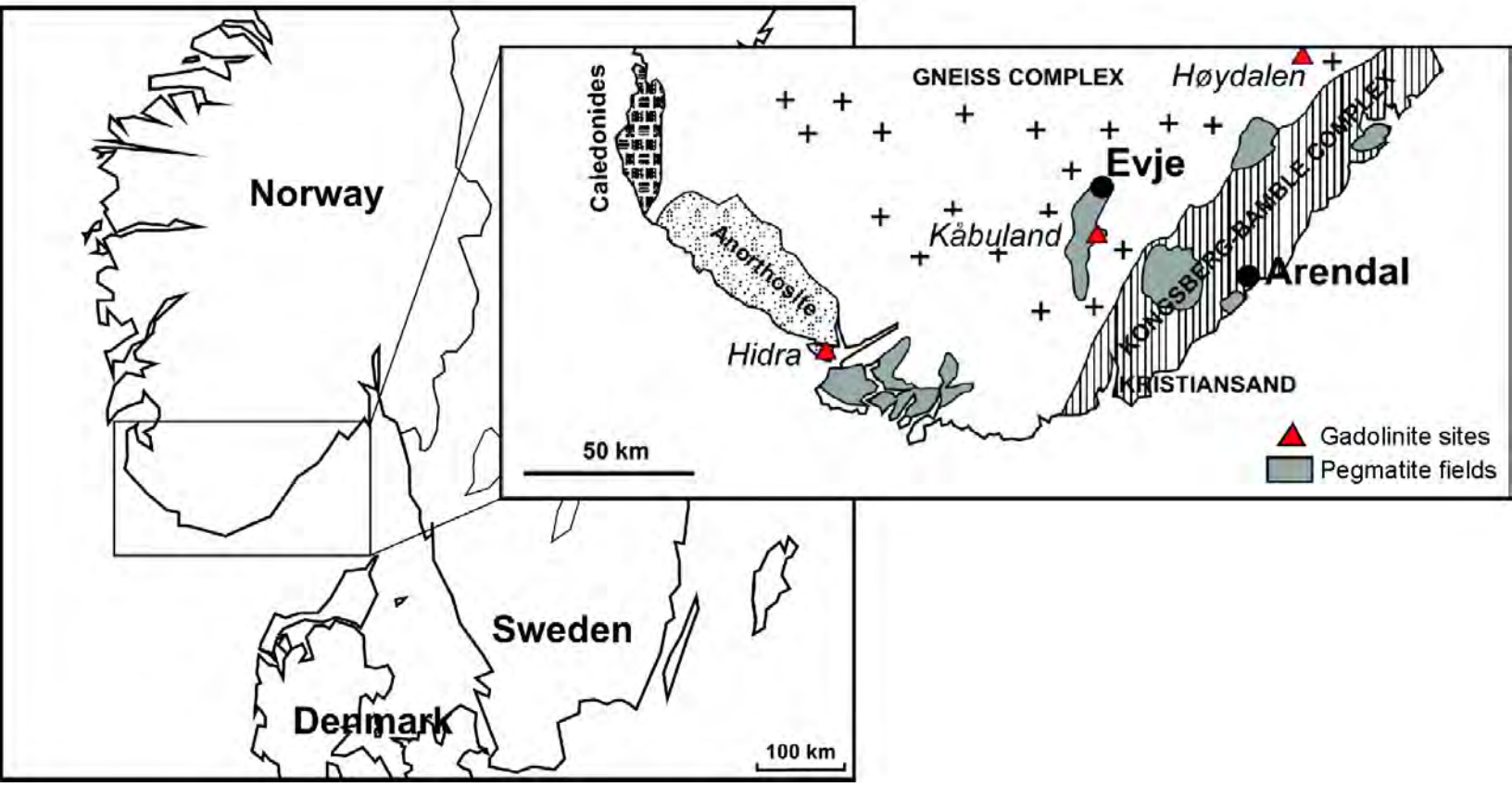
Norway
Sweden
Denmark
100 km
Caledonides
GNEISS COMPLEX
Høydalen
Evje
Kåbuland
Arendal
KONGSBERG-RAMBLE COMPLEX
Anorthosite
Hidra
KRISTIANSAND
50 km
Gadolinite sites
Pegmatite fields

Figure 2

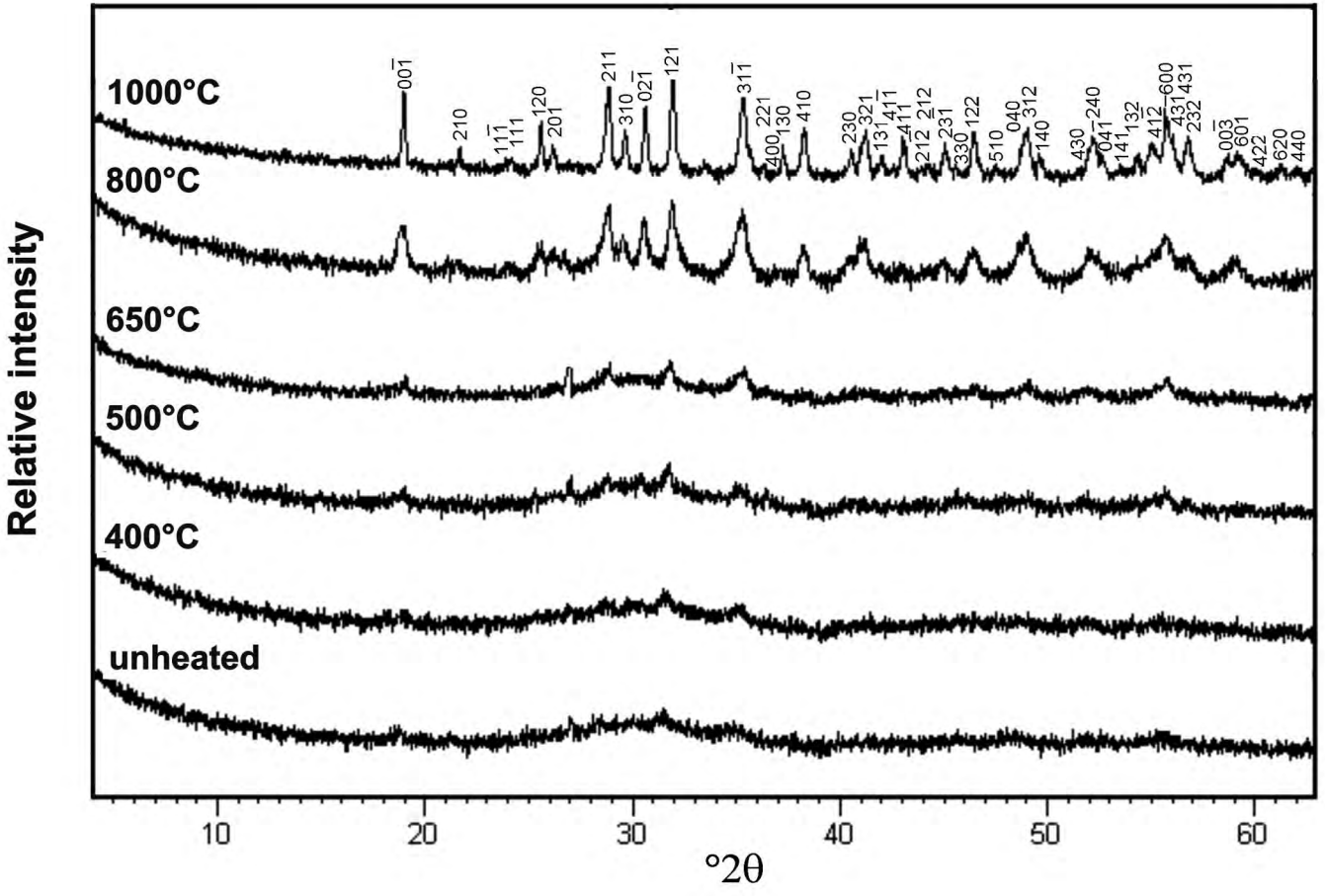
1000°C
800°C
650°C
500°C
400°C
unheated
Relative intensity
°2θ
10
20
30
40
50
60
001
210
111
111
120
201
211
310
021
121
311
221
130
410
230
321
131
411
411
212
212
231
330
122
510
040
312
140
430
240
041
141
132
412
600
431
431
232
003
601
422
620
440

Figure 3

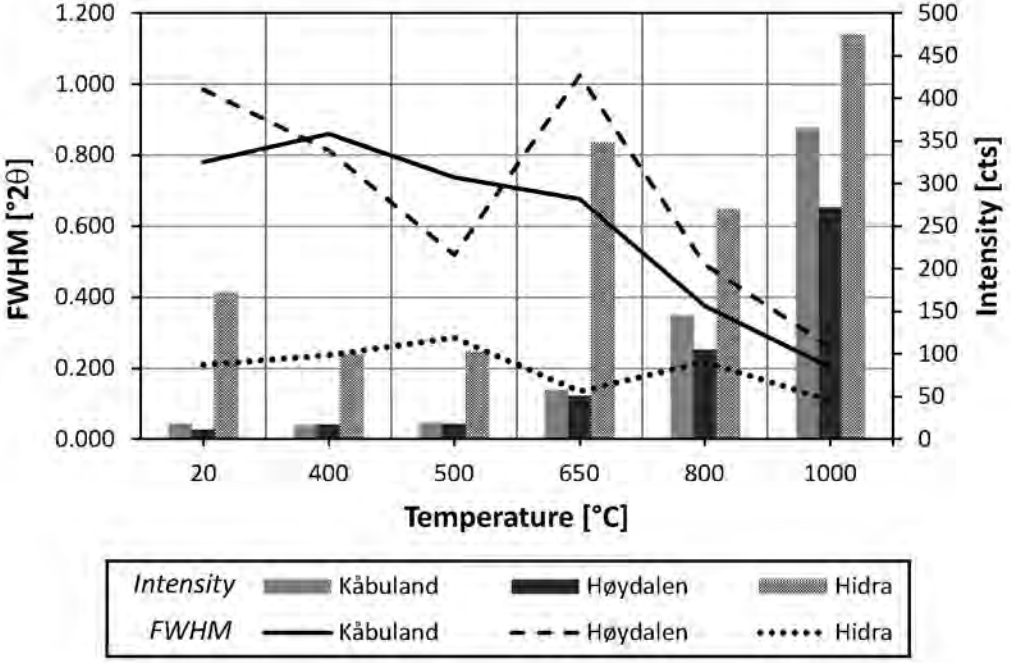
1.200
1.000
0.800
0.600
0.400
0.200
0.000
FWHM [°2θ]
500
450
400
350
300
250
200
150
100
50
0
Intensity [cts]
20
400
500
650
800
1000
Temperature [°C]
Intensity
Kåbuland
Høydalen
Hidra
FWHM
Kåbuland
Høydalen
Hidra

Figure 4

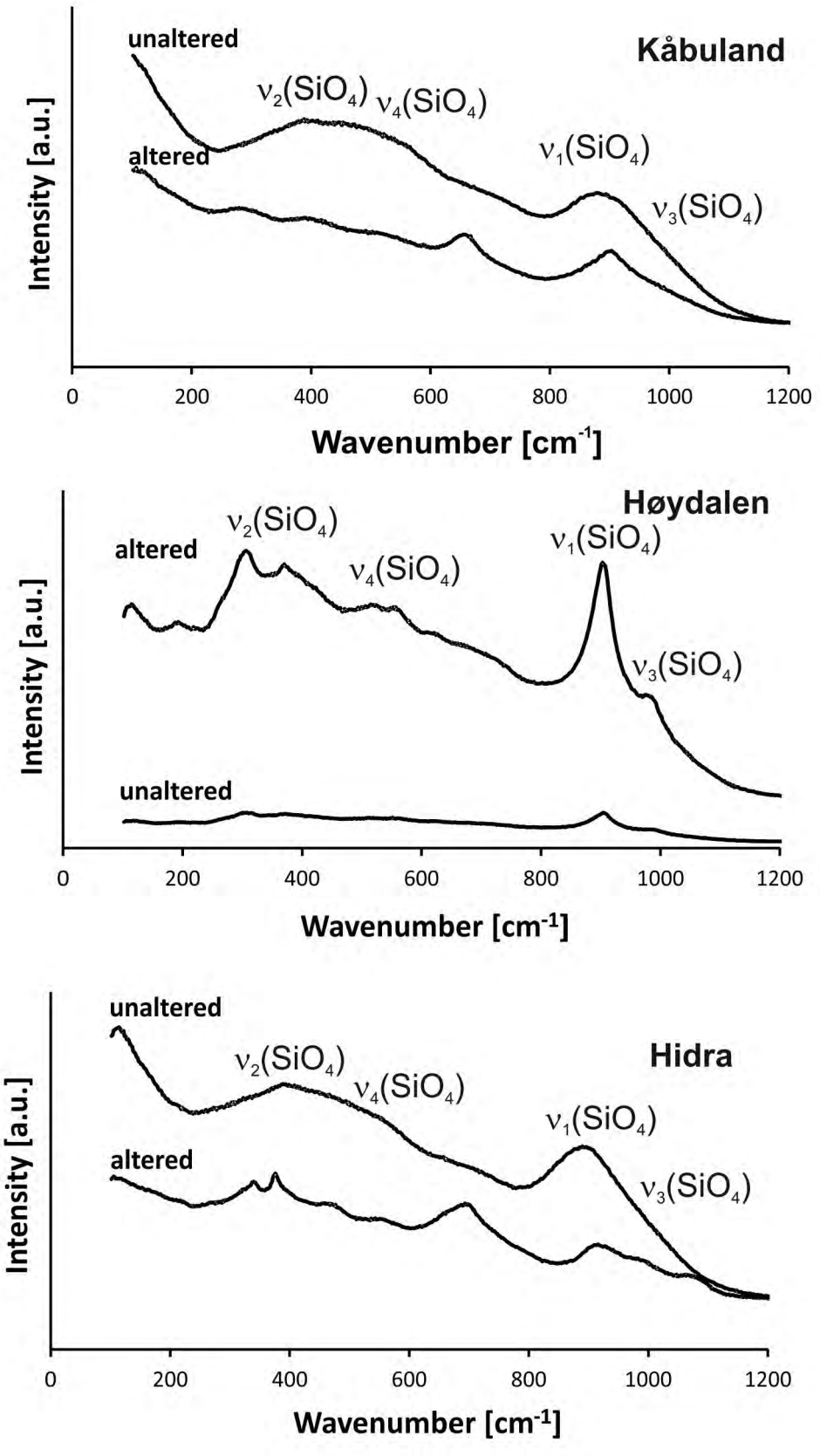
Kåbuland
unaltered
altered
$\nu_2(SiO_4)$
$\nu_4(SiO_4)$
$\nu_1(SiO_4)$
$\nu_3(SiO_4)$
Intensity [a.u.]
0
200
400
600
800
1000
1200
Wavenumber [cm^{-1}]
Høydalen
altered
unaltered
$\nu_2(SiO_4)$
$\nu_4(SiO_4)$
$\nu_1(SiO_4)$
$\nu_3(SiO_4)$
Intensity [a.u.]
0
200
400
600
800
1000
1200
Wavenumber [cm^{-1}]
Hidra
unaltered
altered
$\nu_2(SiO_4)$
$\nu_4(SiO_4)$
$\nu_1(SiO_4)$
$\nu_3(SiO_4)$
Intensity [a.u.]
0
200
400
600
800
1000
1200
Wavenumber [cm^{-1}]

Figure 5

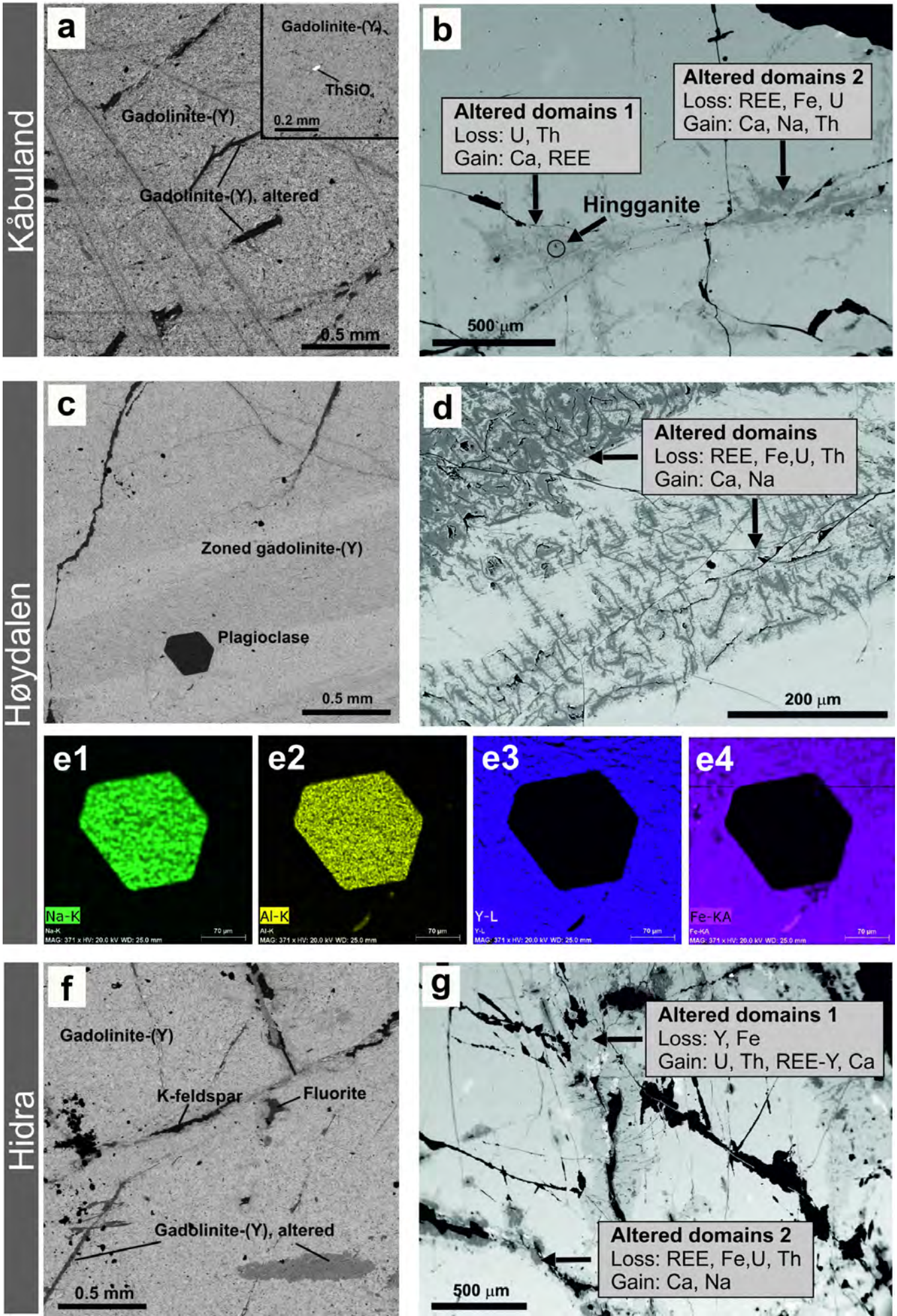
Kåbuland
a
Gadolinite-(Y)
ThSiO4
0.2 mm
Gadolinite-(Y)
Gadolinite-(Y), altered
0.5 mm
b
Altered domains 1
Loss: U, Th
Gain: Ca, REE
Altered domains 2
Loss: REE, Fe, U
Gain: Ca, Na, Th
Hingganite
500 µm
Høydalen
c
Zoned gadolinite-(Y)
Plagioclase
0.5 mm
d
Altered domains
Loss: REE, Fe,U, Th
Gain: Ca, Na
200 µm
e1
Na-K
e2
Al-K
e3
Y-L
e4
Fe-KA
Hidra
f
Gadolinite-(Y)
K-feldspar
Fluorite
Gadolinite-(Y), altered
0.5 mm
g
Altered domains 1
Loss: Y, Fe
Gain: U, Th, REE-Y, Ca
Altered domains 2
Loss: REE, Fe,U, Th
Gain: Ca, Na
500 µm

Figure 6

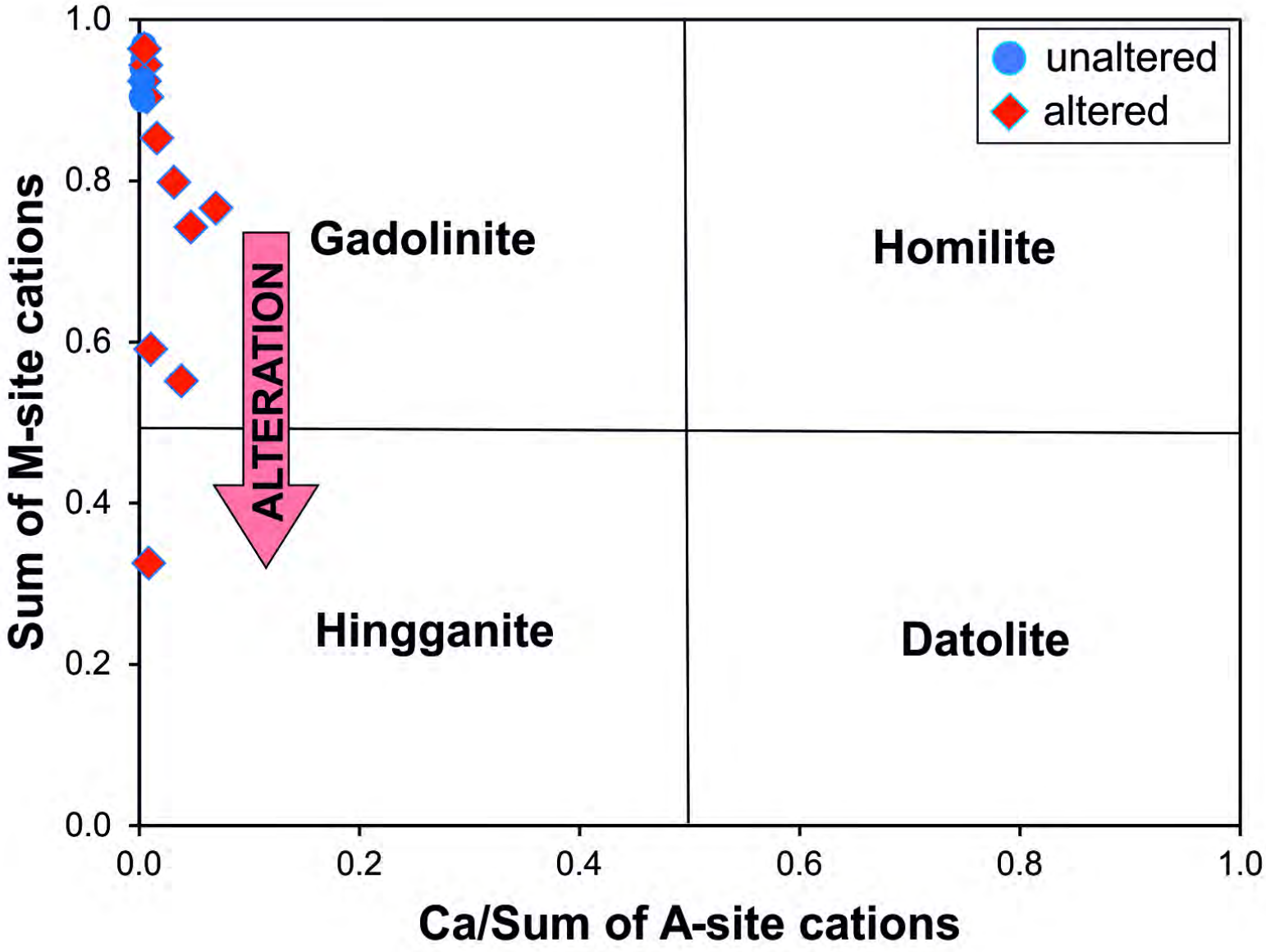
unaltered
altered
Gadolinite
Homilite
Hingganite
Datolite
ALTERATION
Sum of M-site cations
Ca/Sum of A-site cations
0.0
0.2
0.4
0.6
0.8
1.0

Figure 7

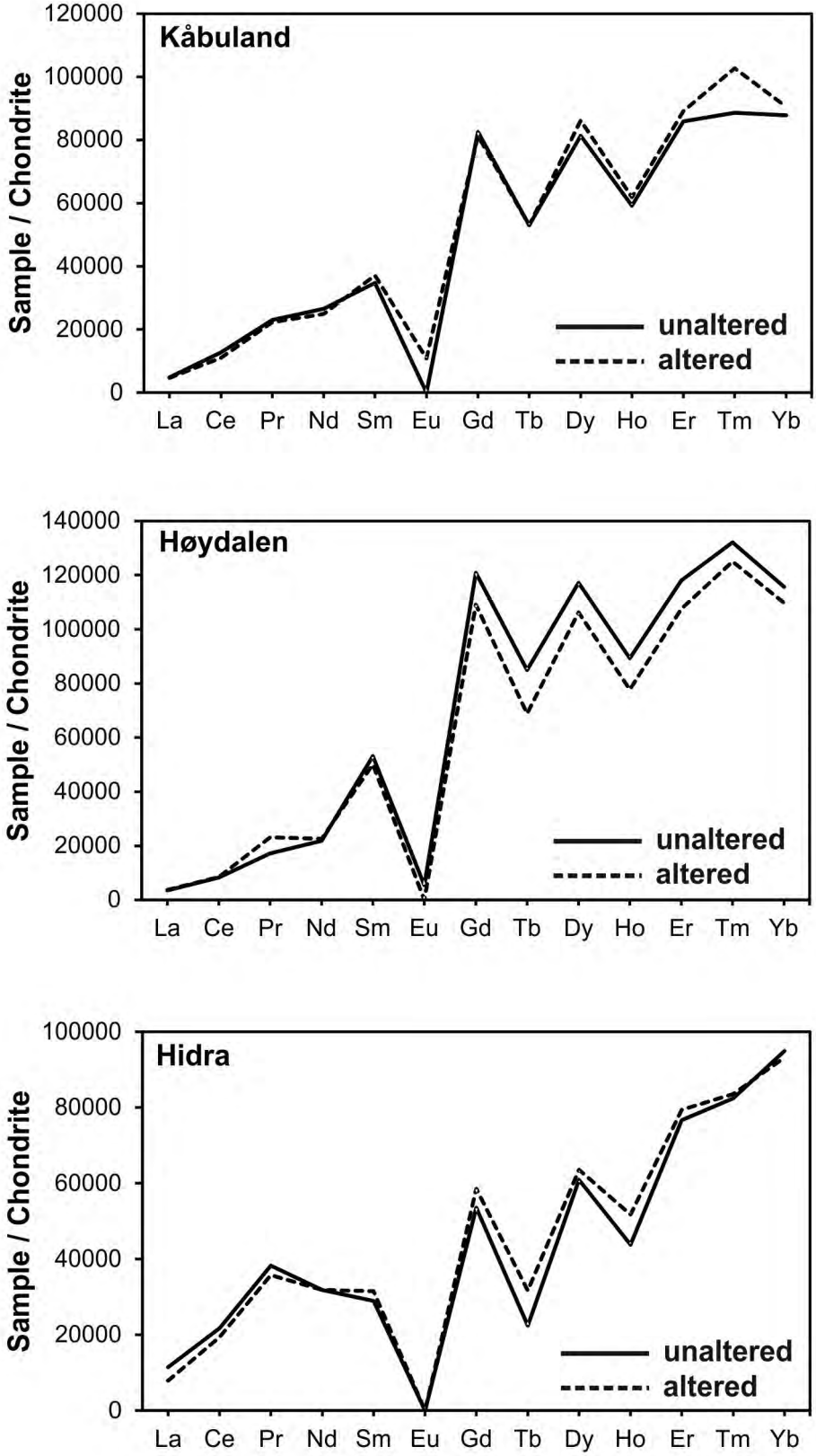
Kåbuland
Sample / Chondrite
120000
100000
80000
60000
40000
20000
0
La Ce Pr Nd Sm Eu Gd Tb Dy Ho Er Tm Yb
unaltered
altered
Høydalen
Sample / Chondrite
140000
120000
100000
80000
60000
40000
20000
0
La Ce Pr Nd Sm Eu Gd Tb Dy Ho Er Tm Yb
unaltered
altered
Hidra
Sample / Chondrite
100000
80000
60000
40000
20000
0
La Ce Pr Nd Sm Eu Gd Tb Dy Ho Er Tm Yb
unaltered
altered